ADVANCED MATERIALS
www.advmat.de

Controlled Nucleation and Oriented Crystallization of Methylammonium-Free Perovskites via In Situ Generated 2D Perovskite Phases

*Yuping Gao, Zonglong Song, Qiang Fu, Yu Chen, Liu Yang, Ziyang Hu, Yongsheng Chen, and Yongsheng Liu**

Enhancing stability while maintaining high efficiency is among the primary challenges in the commercialization of perovskite solar cells (PSCs). Here, a crystal growth technique assisted by in situ generated 2D perovskite phases has been developed to construct high-quality 2D/3D perovskite films. The in situ generated 2D perovskite serve as templates for regulating the nucleation and oriented crystal growth in the α-$FAPbI_3$-rich film. This led to a high film quality with much reduced trap density and an ultralong carrier lifetime. The obtained perovskite film shows excellent stability under extreme environment conditions ($T = 200$ °C, RH = 75 ± 5%). The corresponding PSC achieved an efficiency of 26.16% (certified 25.84%), along with excellent operational stability (T93 > 1300 h, $T \cong 50$ °C) as well as outstanding high and low temperature cycle stability.

1. Introduction

Formamidinium (FA)-based perovskites, such as $FAPbI_3$ or $(Cs_xFA_{1-x})PbI_3$, exhibit suitable bandgaps and promising thermal stability, rendering them ideal candidates for efficient and stable perovskite solar cells (PSCs).[1–3] However, their full potential is yet to be realized due to several challenges, particularly concerning the nucleation and growth of perovskite crystals,[4,5] as well as the stability of perovskite films.[6–8] Although different methods have been reported to tune the crystallization process and enhance the stability of FA-based perovskites, achieving a profound and comprehensive understanding of the nucleation and growth of the perovskite film remains elusive due to rapid crystallization process.[4,9,10] Further investigation is highly necessary to delve into the intricate mechanisms governing the oriented nucleation and crystallization kinetics, allowing for more precise control over the perovskite film formation process.

Layered two-dimensional (2D) perovskites can assist the growth of α-$FAPbI_3$-rich perovskite film, improving its stability, and modulating the crystallization kinetics.[11–14] For example, in 2018, Yang et al. found that incorporating the organic salts, phenethlyammonium iodide (PEAI), into the perovskite precursor solution can protect the FA-based perovskite from moisture invasion, reduce the transition temperature from δ-phase to α-phase of the $FAPbI_3$, and enhance operational stability of the corresponding devices.[11] Subsequently, the template effect of layered 2D perovskites on kinetic-controlled epitaxial growth of $FAPbI_3$ perovskite crystals was further identified.[12] This effect was achieved by inducing strain at the hetero-interface between the 2D perovskites and $FAPbI_3$, which retarded the rate of the perovskite crystals growth. Chao et al. found that a coherent 2D/3D interface could promote epitaxial α-$FAPbI_3$ nucleation, facilitating growth of α-$FAPbI_3$.[13] However, most studies involve directly adding organic spacers to the perovskite precursor solution, which often leads to the nearly simultaneous formation of 2D and 3D perovskites, and the randomly distribution of the 2D phases during the film formation process, hampering the ordered and controlled growth of the perovskites.

Y. Gao, Z. Song, Q. Fu, Y. Chen, Y. Liu
The Centre of Nanoscale Science and Technology and Key Laboratory of Functional Polymer Materials
Institute of Polymer Chemistry
College of Chemistry
Nankai University
Tianjin 300071, China
E-mail: liuys@nankai.edu.cn

Q. Fu
Department of Materials Science and Engineering
City University of Hong Kong
Kowloon 999077, Hong Kong

Y. Chen
Institute of High Energy Physics
Chinese Academy of Sciences
Beijing 100049, China

L. Yang, Z. Hu
Department of Microelectronic Science and Engineering
Ningbo University
Ningbo 315211, China

Y. Chen, Y. Liu
Renewable Energy Conversion and Storage Center (RECAST)
Nankai University
Tianjin 300071, China

The ORCID identification number(s) for the author(s) of this article can be found under https://doi.org/10.1002/adma.202405921

DOI: 10.1002/adma.202405921

Herein, we have developed a novel film fabrication technique, namely in situ generated 2D Perovskite-Assisted Controlled Growth (2D-ACG) technique, that involves in situ generation of 2D perovskites before the formation of FA-based perovskites using a two-step deposition method. Significantly, the in situ generated 2D perovskites were precisely localized and embedded at the top interior surface of the film, instead of being dispersed within the bulk. We monitored the crystallization process of $FAPbI_3$-rich perovskites and found that this 2D-ACG technique could effectively regulate the crystal orientation and crystallization kinetics of the perovskite film during both the nucleation and growth processes, resulting in the production of larger-sized, higher quality perovskite crystals and the released residual strain, thereby enhancing the overall photovoltaic performance of the devices. Specifically, the obtained perovskite film shows excellent stability under extreme environment conditions (T = 200 °C, RH = 75 ± 5%) in comparison control film, resulting in outstanding operational stability (T93 > 1300 h, T = ~50 °C) and high- and low-temperature cycle stability for the corresponding devices.

2. Results and Discussion

Typically, the nucleation and growth of 3D perovskite films with assistance from conventional 2D perovskites involve adding the organic spacers to the lead iodide (PbI_2) precursor solution or to a mixed organic ammonium solution, using a two-step film-deposition protocol (Figure S1, Supplementary Information). This method often results in the random distribution of the 2D perovskite phases within the 3D perovskite film.[15–18] Here, we developed a 2D-ACG technology for the fabrication of $FAPbI_3$-rich 2D/3D perovskite film, as illustrated in **Figure 1A**. A unique aromatic organic salts, namely 4,5,6,7-tetrahydrothieno[3,2-c]pyridine hydroiodide (ThPyI), was developed as a representative example to construct the layered 2D perovskite seeds (Figure 1B,C). Its lager in-plane Pb–I–Pb angle (θ_{in} = 174°) at the coherent interface with α-$FAPbI_3$ were beneficial for the growth and stabilization of α-$FAPbI_3$ at the 2D/3D coherent interface (Figure 1D and Figure S2a, Supplementary Information).[13] In contrast, most 2D perovskites exhibit an in-plane Pb–I–Pb angle (θ_{in}) smaller than 155° as illustrated in Figure S2b with PEA, PMA, and BA as spacers.[13] These θ_{in} values differ from that of α-$FAPbI_3$ by over 25°. We initiated the process by spin-coating the organic spacer (ThPyI) solution onto the annealed PbI_2 film. Upon contact with the PbI_2 film, the bulky organic spacer undergone an in situ reaction with the surface-layer of PbI_2, spontaneously forming a 2D perovskite layer as confirmed by the X-ray diffraction (XRD) patterns in Figure 1E and photoluminescence (PL) spectra in Figure S3 (Supplementary Information). As shown in Figure 1F,G, the top view field-emission scanning electron microscopy (SEM) image revealed a discontinuously island-like distribution of the 2D perovskite on the surface of PbI_2 film. The localized 2D perovskite could play a crucial role as template, facilitating the oriented nucleation and controlled growth of α-$FAPbI_3$ perovskite. The XRD patterns in Figure 1H show that the relative intensity of the (110) planes of the perovskite film treated with 2D-ACG, referred to as the target-1 film, was stronger than that of control films (perovskite films without 2D-ACG treatment), suggesting improved crystallinity. Furthermore, the target-1 film exhibited a compact, pinhole-free morphology with increased average grain sizes over 1 µm compared to the control film (≈ 500 nm) (Figure 1I,J). The improved crystal quality of the film was further verified by cross-sectional SEM images, which showed complete penetration between the top and bottom electrodes with excellent connection and orientation (Figure S4, Supplementary Information).

To investigate the longitudinal distribution of 2D perovskite within the PbI_2 film, we conducted cross-sectional SEM and depth-dependent grazing incidence wide-angle X-ray scattering (GIWAXS) measurements. The cross-sectional SEM images of the PbI_2 film treated with ThPy spacer verified the presence of a 2D perovskite layer with a thickness of ≈70 nm (**Figure 2A**). Analysis of the integrated area under the (002) peak (representing 2D perovskite, n = 1) and the (001) peak (representing PbI_2) from the GIWAXS spectra at various incident angles (Figure S5, Supplementary Information) supported the localized and embedded distribution of the 2D perovskite (Figure 2B). The GIWAXS data revealed that within the top 20 nm, as estimated from the penetration depth curve (Figure S5, Supplementary Information) (α_i = 0.16°) of the film, the predominant phase was 2D perovskite, indicating a high concentration of 2D phase near the surface.[19] At a depth of 75 nm (α_i = 0.2°), the intensity of the 2D perovskite peak reached its maximum and then started to decrease, marking the critical depth or critical angle. This finding suggests that the distribution of 2D perovskite was within ≈75 nm depth from the surface, in line with the cross-sectional SEM analysis.[20] Additionally, at the critical depth of the 2D phase, the intensity of the PbI_2 peak started to increase significantly, almost reaching the same level as the 2D perovskite peak. This observation suggests that the 2D perovskite was localized and embedded within the interior of PbI_2 film near its upper surface. At a depth of ≈200 nm (α_i = 0.4°), the intensity of the 2D perovskite peak started to decrease, while the PbI_2 peak continued to strengthen, indicating a reduction in the 2D perovskite, primarily due to the limited penetration of the organic spacer solution. We extended the perovskite fabrication by spin-coating organohalide salts (FAI/MACl, 90 mg: 9 mg in 1 ml IPA) onto the PbI_2 film with localized 2D perovskites and investigated the distribution of the 2D phase in the perovskite film before annealing. Interestingly, the critical angle for the 2D phase in the perovskite film shifted to 0.4° (Figure 2C), corresponding to a critical depth of about 200 nm. This shift could be attributed to the lattice expansion caused by the formation of the 3D perovskite phase. Cross-sectional SEM showed a perovskite film thickness of up to 900 nm (Figure S4, Supplementary Information), significantly greater than the 550 nm thickness of the PbI_2 film (Figure 2A). This result confirmed that the 2D perovskite was localized and embedded within the interior of the 3D perovskite film near its upper surface before annealing, serving as a template to regulate the crystallization kinetics of the 3D phase.

To gain deeper insight into the role of 2D perovskite in the crystallization of $FAPbI_3$ perovskite films from precursors, we used synchrotron-based in situ probes to monitor the structure evolution of the films at room temperature. As shown in Figure 2D and 2E, azimuthally integrated in situ 2D GIWAXS measurements was taken during the perovskite film forming process. Upon the dropwise addition of the organic ammonium salt solution onto the ThPy-processed PbI_2, we observed the

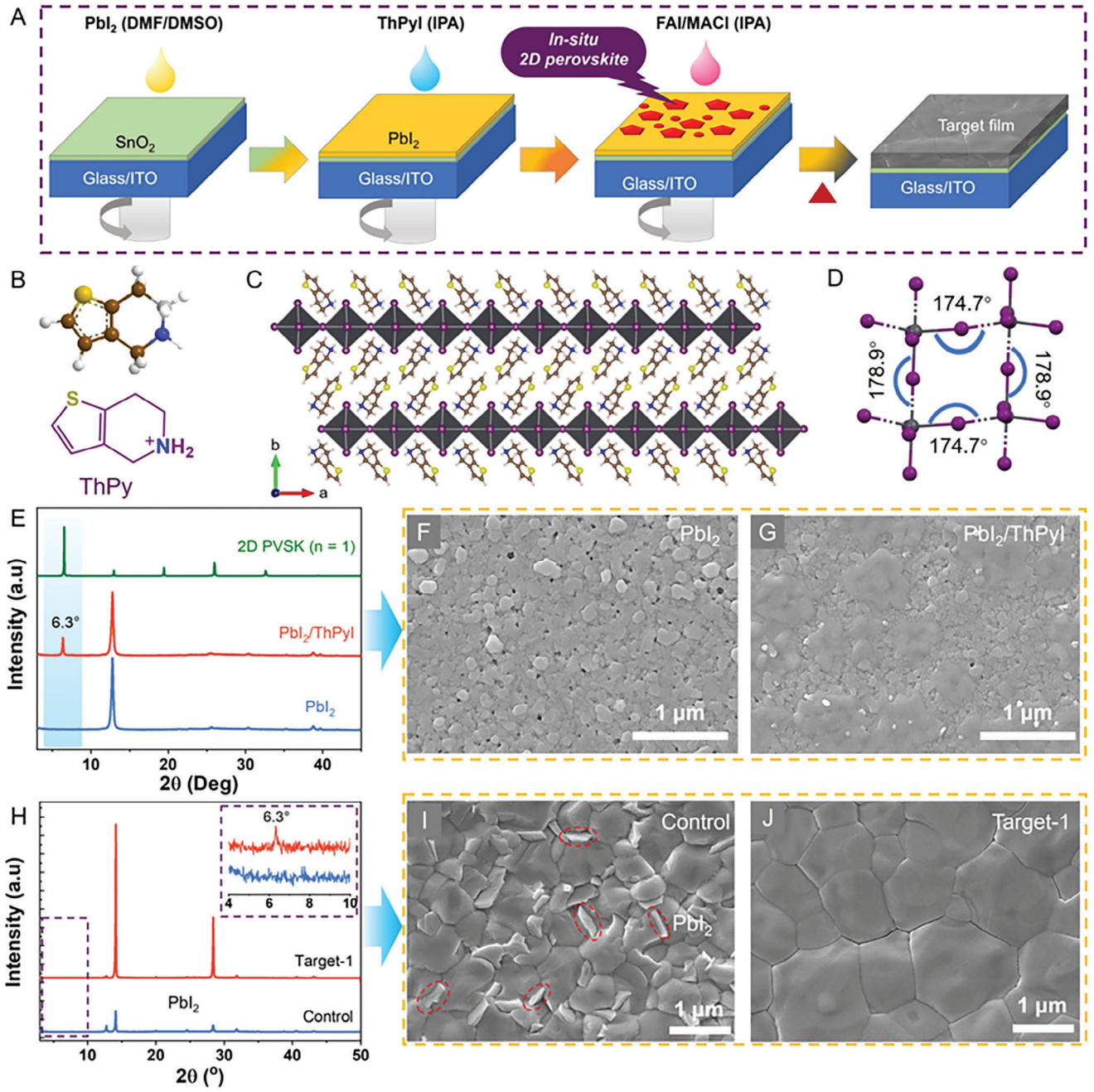

Figure 1. Schematic diagram of the 2D-ACG technique and the in situ formation of 2D phase. A) Schematic fabrication process of the perovskite film with the in situ generated and embedded 2D perovskite-assisted controlled growth (2D-ACG) technique. B) The molecule structure of ThPy and C) the single crystal structure of the 2D perovskite of $(ThPy)_2PbI_4$. D) The in-plane (θ_{in}) and out-plane Pb–I–Pb angle of $(ThPy)_2PbI_4$. E) XRD patterns of the 2D perovskite film [$(ThPy)_2PbI_4$, green line] and PbI_2 film with (red line) and without (blue line) organic spacer deposition. Top-view SEM images of PbI_2 films F) without and G) with organic spacer deposition. H) XRD patterns of perovskite films with (red line) and without (blue line) 2D-ACG treatment. Top-view SEM images of perovskite films I) without and with J) 2D-ACG treatment.

disappearance of the PbI_2 peak, accompanied by the emergence of the perovskite (110) diffraction peak. However, the α-phase peaks only persisted for a few seconds before gradually fading away, indicating the instability of the α phase under ambient conditions. Generally, the formation of α-$FAPbI_3$ requires a heating temperature above 150 °C to achieve a corner-sharing $[PbI_6]^{4-}$ octahedral structure.[21–23] Presumably, the initial appearance of the α-phase during the spin-coating process could be attributed to the MACl-induced kinetic effect, as confirmed by the XRD measurements.[4,24] As shown in Figure S6k (Supplementary Information), the XRD data shows no obvious α-$FAPbI_3$ peaks. Conversely, a distinct α-$FAPbI_3$ peaks was observed after the

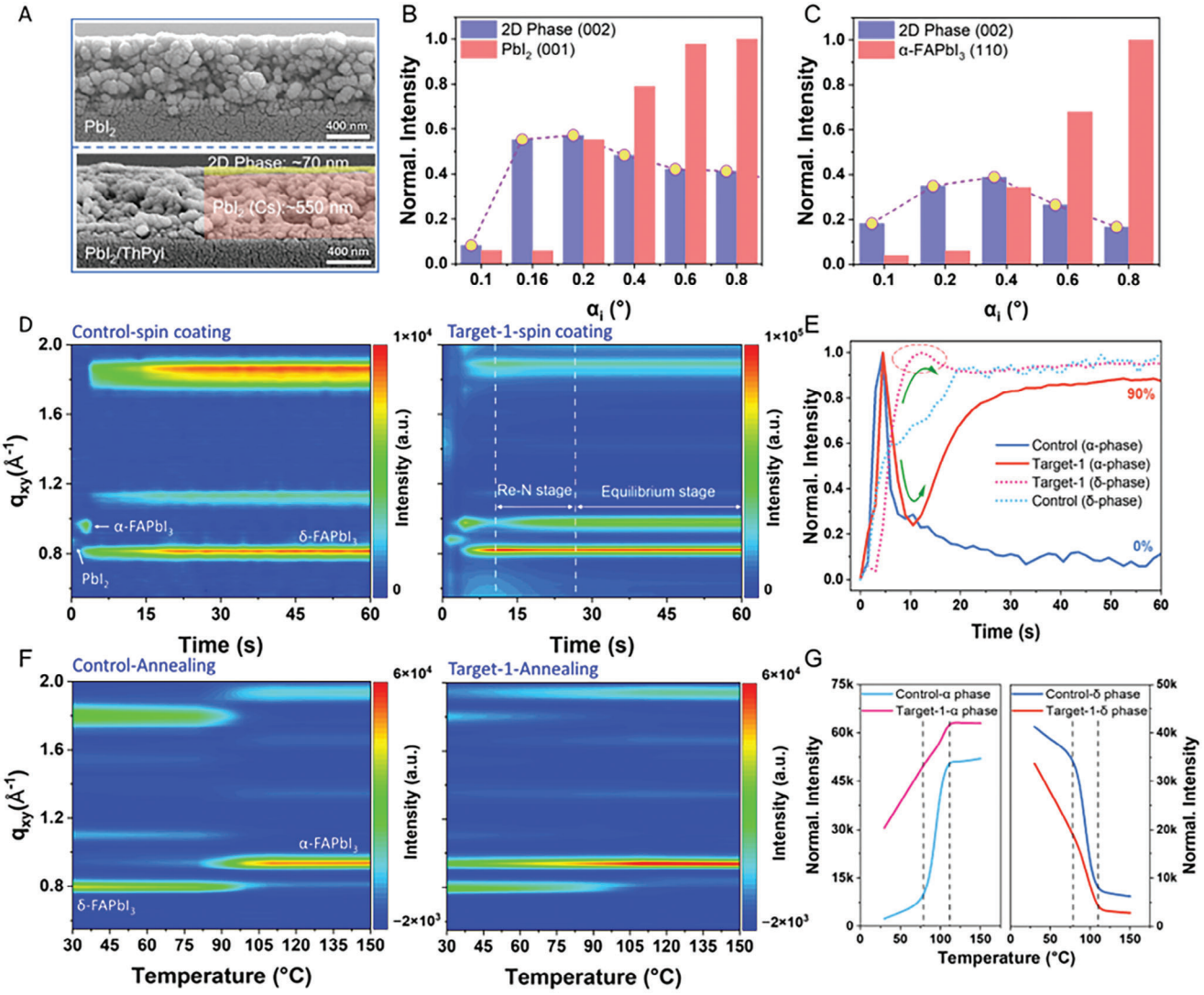

Figure 2. Nucleation and crystallization dynamics of perovskite films. A) Cross-sectional SEM images of PbI_2 films without (upper) and with (down) organic spacer deposition. B) Amount of 2D perovskite and PbI_2 materials in the PbI_2 film extracted from the angular integrated diffraction peaks of the GIWAXS spectra. C) Amount of 2D perovskite and α-$FAPbI_3$ materials in wet perovskite film extracted from the angular integrated diffraction peaks of GIWAXS spectra. D) The structural evolution of the perovskite during the spin-coating stage when the organohalide salts solution was dropped onto redeposited PbI_2 film by azimuthally integrated in situ 2D GIWAXS. E) The integrated intensity of α-$FAPbI_3$ and δ-$FAPbI_3$ during the spin-coating process extracted from 2D GIWAXS over time. F) The structural evolution monitored by azimuthally integrated in situ GIWAXS during heating from RT to 150 °C using the as-deposited thin films. G) The integrated intensity of α-$FAPbI_3$ and δ-$FAPbI_3$ during the annealing process extracted from 2D GIWAXS over time.

addition of sufficient MACl. As the α phase gradually disappeared, the (100) diffraction peaks of the δ-phase began to emerge and progressively strengthen. Notably, while the δ-phase in the control group continued to increase, the corresponding peak intensity of the δ-phase in the target-1 group started to decrease after 10 s, accompanied by a gradual increase in the α-phase peak (Figure 2E). This phenomenon is described as a renucleation process (Re-N stage), during which the disappearance, formation and growth of the nuclei occur almost simultaneously. A noteworthy observation was that the entire process extended for almost 15 s, suggesting that the rate of the re-nucleation related to 2D perovskites was much slower compared to that at the initial stage of the spin-coating, which was maintained for a brief 4.5 s duration. The sluggish re-nucleation kinetics proved beneficial in reducing defects and improving the quality of the film, as confirmed by the larger grain sizes in SEM images and increased diffraction peak intensity in XRD patterns. This result indicates that the growth of the α-phase perovskite film was kinetically affected by the presence of the localized 2D perovskite. Simultaneously, the 2D phases reduced the δ-phase to α-phase transition temperature and enhanced the stability of α-phase. In this process, the 2D phase disconnected the face-sharing $[PbI_6]^{4-}$ octahedra of δ-phase at the coherent interface, transforming it into the corner-sharing structure of the α-phase.[13] Subsequently, this transformation propagated toward bulk regions, as confirmed by depth-dependent GIWAXS measurement (Figure 2C).[6,13]

The χ-pole figure of the perovskite (110) plane in Figure S7 (Supplementary Information) was generated using GIWAXS during the nucleation stage to study the orientational preference of α-$FAPbI_3$ perovskite.[19,25–27] The orientation distribution of the control perovskite film shows two-peak patterns around −55° and +55° (Figures S6 and S7, Supplementary Information). However, a sharp peak concentrated at a polar angle of 0° was observed for the target-1 group throughout the spin-coating process, indicating a nucleation stage (including first nucleation and re-nucleation stage) with a preferred out-of-plane orientation along the (110) facet, favoring vertical carrier transport (Figure S8, Supplementary Information).[16,28] The preferentially oriented nucleation mechanism controlled the subsequent crystal growth aligned with the preferred orientation along the (110) facet. As aforementioned, the 2D perovskite could influence the crystallization kinetics of $FAPbI_3$-rich perovskite films. We speculated that the oriented nucleation is a direct consequence of the oriented 2D perovskite. The out-of-plane orientated 2D perovskite played a pivotal role in initiating and guiding the nucleation stage, resulting in a meticulously controlled process of crystal nucleation and growth (Figure S5, Supplementary Information).

In situ GIWAXS experiments were performed to monitor the annealing process of the wet perovskite films during heating from room temperature (RT) to 120 °C, aiming to elucidate the structural changes throughout the entire crystallization process. In the control group, δ-phase of the $FAPbI_3$-rich perovskite underwent a phase transition to the α-phase, initiating at 80 °C and completing at 105 °C (Figure 2F). Within this narrow temperature range, both nucleation and crystallization processes of the α-phase occurred. In contrast, the nucleation stage (Re-N stage) of α-$FAPbI_3$ was first formed prior to the annealing stage by the template effect of the 2D perovskite during the spin-coating process. Consequently, these nucleation sites, along with the 2D perovskite, act as seeds, facilitating the crystalline growth of the α-phase during the annealing process until completion at 105 °C. Notably, in the target-1 group, crystal growth occurred considerably slower compared to the control group, spanning from RT to 105 °C. Figure 2G illustrated the corresponding variation curve of perovskite phases with temperature. In the control film, both α-phase and δ-phase intensities exhibit a sharp transition from 80 to 105 °C. In contrast, the target-1 film experienced a gradual increase in α-phase intensities and a decrease in δ-phase intensities until reaching equilibrium at 105 °C. This observation underscores that, in contrast to the control film, the transition from the δ-phase to the α-phase for target film occurred at a slower pace, with the 2D perovskite effectively modulating the crystalline growth kinetics of the α-$FAPbI_3$. The synergistic effect of the slower crystalline growth process and preferentially oriented nucleation could facilitate the preparation of controlled and oriented perovskite films. As shown in **Figure 3**A–C, it is evident that the target-1 film, after annealing, demonstrates a preferred out-of-plane direction along the (110) facet, consistent with the crystal orientation observed during the nucleation stage. In contrast, the control film, after annealing, maintains the preferential orientation at around ±55° observed during the nucleation stage. In addition, the control perovskite film exhibits bright reflections at the scattering vector $q = 9\ nm^{-1}$, which was assigned to the (001) plane of PbI_2. However, the target-1 film shows no obvious diffraction ring of PbI_2. This is consistent with the observed results from XRD and SEM results, providing evidence that the presence of 2D perovskite alteres the crystalline growth process and stablizies the α-$FAPbI_3$.

Through depth-resolved GIWAXS measurements, we further investigated the strain distribution within the film. As the incident angle changed from 0.2° to 1.05°, the diffraction patterns of the control perovskite gradually shift toward a larger value (Figure 3D), demonstrating the existence of compressive strain in the perovskite film around the region closer to the substrate. In contrast, the q_z values in target-1 film almost invariant suggesting that the lattice strain relaxed induced by 2D-ACG strategy (Figure 3E). In detail, we calculated the slopes of the corresponding fitted line of q_z values and grazing incidence angle for both perovskite films. As shown in Figure 3F, the slope of the film prepared by the 2D-ACG strategy is 0.0032, much lower than that of the control system (0.0118). The released residual strain could be attributed to the controlled nucleation and oriented crystallization of perovskite films, which is inextricably linked to the in situ formation of localized 2D phases as illustrated in Figure 3G.

To reduce the surface defects and improve the stability of the perovskite film, a structured 2D/(2D/3D) structure by spin-coating isopropanol (IPA) solution of ThPyI onto the target-1 film was created and named as target-2 film. The GIWAXS data in Figure 3A,B and Figure S9 (Supplementary Information) show that, in contrast to the control and target-1 films, the target-2 film exhibits an obvious (002) Bragg spot of the 2D perovskite phase ($n = 1$) in the small q-value region, suggesting the successfully formation of 2D perovskite on top of target-2 film. Note that the incorporation of the 2D perovskite layer on top of target-1 film can effectively protect against external moisture erosion and further enhance the inherent stability of the perovskite film.[20,29,30] Additionally, we observed that the spontaneous formation of the surface 2D phase did not require high-temperature annealing. Simply spin-coating the ThPyI solution onto the film surface was enough to induce the formation of the 2D perovskite layer. This behavior contrasts with that of PEAI, where annealing is necessary for the formation of the 2D phase.[31] Such a characteristic provides convenience for the development of the 2D-ACG strategy described in this study. We further studied the effect of the 2D perovskite layer on the energy-level alignment at the interface using ultraviolet photoelectron spectroscopy (UPS). Work functions of the control, target-1, and target-2 perovskites were estimated as 4.09, 4.30, 4.37 eV, respectively (Figures S10 and S11, Supplementary Information). In comparison with the control film, the Fermi levels of the target-1 and target-2 films were found to be closer to the valence band edge, indicating enhanced p-type characteristics.[32] In addition, the target-1 and target-2 films demonstrated a higher potential compared to the control film, as assessed by Kelvin probe force microscopy (KPFM) (Figure S12, Supplementary Information). This enhancement can be ascribed to the reduced surface electronic trap density and enhanced p-type characteristics. Furthermore, the potential distribution of the target-1 and target-2 films was ≈75 and 62 mV, respectively, representing a decrease compared to the control film (≈90 mV) (Figure S12D, Supplementary Information). These results are expected to improve charge separation and transport efficiencies within the bulk perovskite film and at the interface between the perovskite and hole transport layer, thereby reducing the nonradiative recombination losses.[33,34] The suppression of

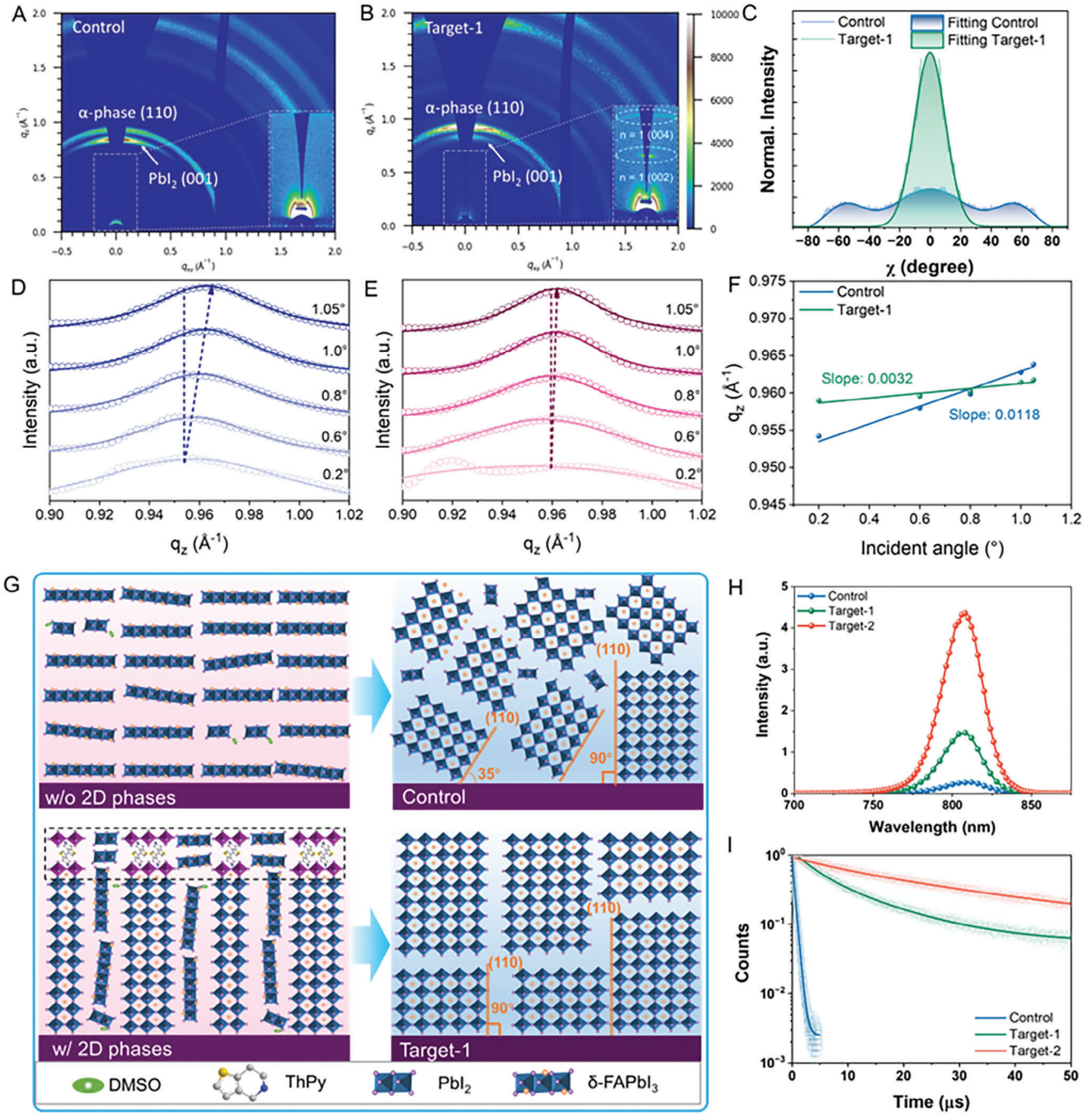

Figure 3. Structural and optical spectroscopic characterization of perovskite films. 2D GIWAXS images of the A) control and B) target-1 perovskite films after annealing. C) The χ-pole figures of the perovskite (110) plane constructed from the 2D GIWAXS of the control and target-1 perovskite films after annealing. Grazing-incident wide-angle X-ray scattering profiles of D) control and E) target-1 perovskite films with the angle of incident beam ranging from 0.2° to 1.05°. F) The q_z values obtained from (110) plane as a function of incidence angle. G) Schematic illustration of the oriented nucleation and growth of perovskite films facilitated by the in situ 2D perovskite phases. H) Steady-state PL and I) time-resolved PL spectra of the perovskite films.

nonradiative recombination loss was further verified by the enhanced steady-state photoluminescence (PL) intensity of the target-1 and target-2 films (Figure 3H).[3,35] Furthermore, time-resolved photoluminescence (TRPL) analysis revealed a significant increase in perovskite lifetime, from 0.46 μs for the control film to 10.44 μs for the target-1 film (Figure 3I and Table S1, Supplementary Information). Additionally, the lifetime was further extended to ≈27.58 μs for target-2 film. These results suggested that the localized 2D perovskite effectively reduced the defect concentration within the perovskite film, and the surface defect is further reduced by the introduction of the 2D passivation layer.

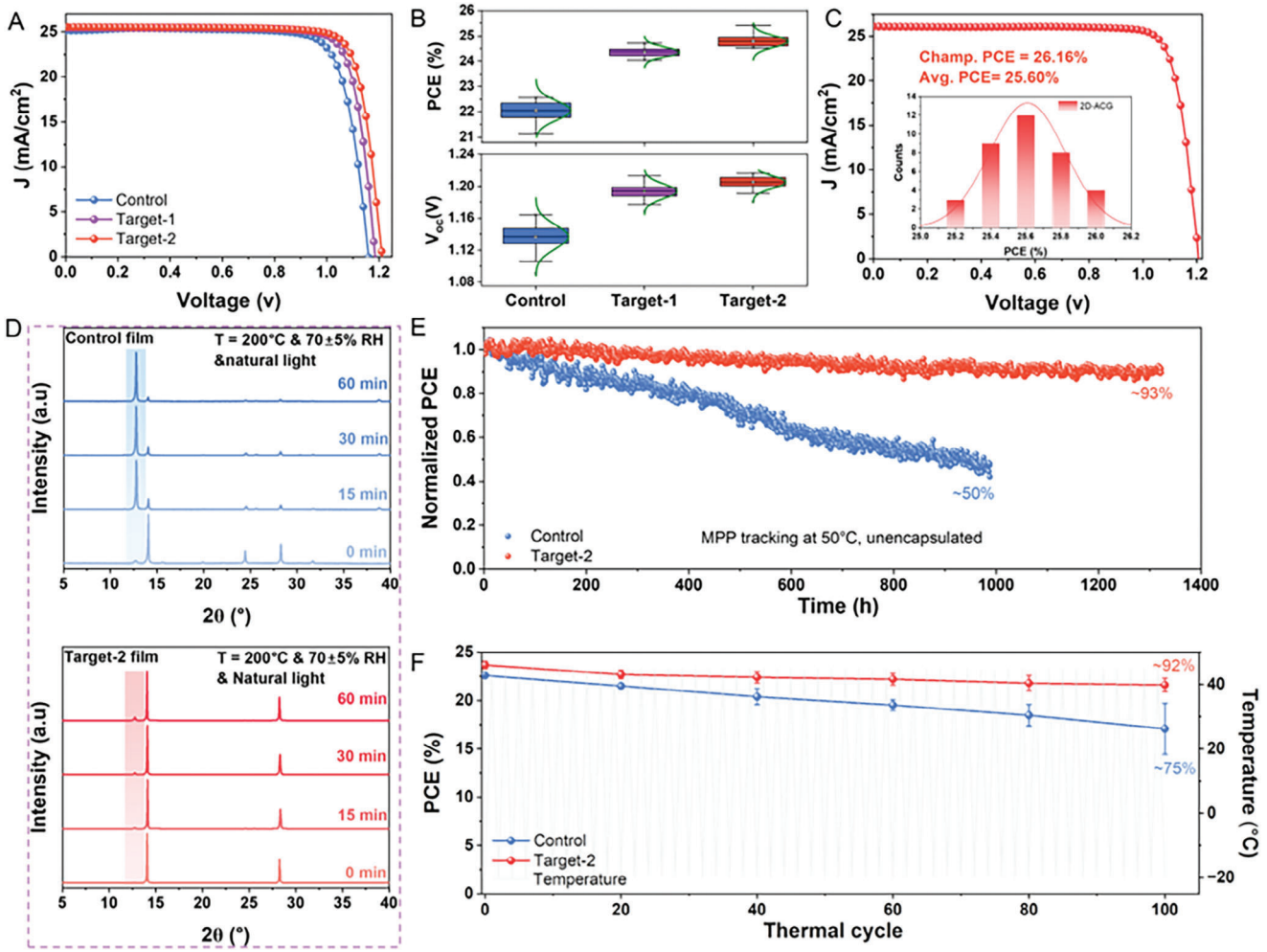

Figure 4. Photovoltaic performance and stability of devices. A) The typical *J–V* curves of the perovskite photovoltaic devices. B) PCE and V_{OC} distribution of perovskite solar cells. C) Best device performance of target-2. Inset) PCE distribution for the best device and 35 devices data are collected. D) Evolution of XRD patterns of the control and target-2 perovskite films under rigorous conditions (200 °C, RH 75 ± 5%, Natural light). E) MPP tracking of the unencapsulated devices under continuous light illumination at 50 °C in N_2. F) Thermal cycling stability of perovskite solar cells. The rapid thermal cycle was executed by placing the devices in an environment at −20 °C, followed by transferring them to a hot plate set at 45 °C. Each stage lasted for 3 min to achieve thermal equilibrium.

Subsequently, we conducted an evaluation of the photovoltaic performance of the fabricated perovskite solar cells. As shown in the current density–voltage (*J–V*) characteristics of the devices in **Figure** 4A, the target-1 devices (fabricated using the target-1 film) demonstrated significantly improved power conversion efficiency (PCE) of 24.72%, while the best control device achieved a PCE of only 23.32%. After passivation using 2D perovskite, the device (target-2) efficiency was further enhanced to 25.42%, with an open-circuit voltage (V_{OC}) of 1.212 V and a fill factor (*FF*) of 82.19% (Table S2, Supplementary Information). The V_{OC} loss for the champion device was calculated to be ≈0.33 V (E_g = 1.54 eV, Figure S16, Supplementary Information), which was among the lowest V_{OC} loss reported for PSCs so far.[17,36] The enhancement in V_{OC} was further verified through capacitance–voltage (C–V) measurements following the Mott–Schottky relationship (Figure S18A, Supplementary Information). The target-1 and target-2 devices displayed a higher built-in voltage (V_{bi}) compared to the control devices, signifying a more robust driving force for charge separation in target-1 and target-2 devices. The enhanced V_{OC} was further evaluated using the emission yield of the electroluminescence spectra (EQE_{EL}). When the injection current density was set equal to short circuit current density (J_{SC}) under solar illumination, the control device exhibited an EQE_{EL} value of 0.73%. In contrast, EQE_{EL} of the target-1 and target-2 devices were improved to 2.35% and 4.53%, respectively (Figures S18B and S18C, Supplementary Information). Employing the equation $\Delta V_{OC} = (k_B T/q)\ln(EQE_{target\text{-}2}/EQE_{control})$,[37] the estimated V_{OC} improvement for target-2 was 47 mV, aligning well with the experimentally observed V_{OC} variation in the devices. The remarkable enhancement in PCE mainly reflected in the improved V_{OC} and *FF*, which was ascribed to the suppressed nonradiative recombination and the reduced carrier extraction-transport barrier at the interface. This was evidenced by the light dependence of V_{OC} (Figure S19, Supplementary Information), where the target-1 and target-2 device exhibits significantly lower slopes of 1.70 and 1.62 kT/q, respectively, compared to the control device's slope

of 1.89 kT/q.[14] To gain deeper insights into charge-carrier lifetimes in fully operating devices, we conducted transient photovoltage (TPV) measurements under open-circuit conditions. As shown in Figure S20a (Supplementary Information), the charge recombination time constants (τ) increased from 230 µs in the control device to 349 µs and 459 µs for the target-1 and target-2 devices, respectively. This significant increase in carrier lifetime for the target-2 device indicates slower charge recombination, suggesting that incorporating 2D perovskite reduces nonradiative recombination.[14] Additionally, transient photocurrent (TPC) decay under short circuit conditions revealed decay times of 5.05 µs for the control, 4.87 µs for target-1, and 4.03 µs for target-2 devices (Figure S20b, Supplementary Information). The shorter decay time in the target-2 device suggests more efficient charge extraction, likely due to reduced interfacial charge accumulation and recombination.[14] The statistical distribution of PCEs for 36 devices are presented in Figure 4B, confirming the highly reproducible performance improvements achieved by incorporating 2D perovskite.

To minimize light reflection and maximize photocurrent, we opted for an antireflective coating of magnesium fluoride (Table S3, Supplementary Information). Consequently, the PCE of Target-2 was further boosted to 26.16% for the best device (Figure 4C and Table S4, Supplementary Information), with a certified PCE of 25.84% (Figure S21, Supplementary Information). The integrated J_{SC} from EQE curves was 25.32 mA/cm^2 for target-2 devices, matched well with the corresponding J_{SC} values (<3.0% deviation) in J–V curves (Figure S22). To assess the stability of the perovskite film, unencapsulated perovskite films were subjected to rigorous conditions (200 °C, RH 75 ± 5%, Natural light), and their XRD patterns were monitored. As illustrated in Figure 4D, the control perovskite film has almost completely decomposed after 60 min. In contrast, the target-2 film maintained its original structural composition, highlighting its excellerent thermal and humidity stability. To assess long-term operational stability, unencapsulated devices underwent maximum power point (MPP) tracking under continuous light illumination (100 ± 10 mW cm^{-2}, white LED) in an N_2 atmosphere (Figure 4E). The control device dropped to ≈50% of its original PCE after 1000 h, while the target-2 device retained over 93% of its initial efficiency after more than 1350 h at 50 °C. Subsequently, the encapsulated devices were aged under rapid thermal cycling between −20° and +45 °C. As illustrated in Figure 4F, following 100 thermal cycles, the control device suffered a severe decline to 75% of its original performance, whereas the target device retained 92% of its initial value.

3. Conclusion

We have developed an efficient technique, namely 2D-ACG technique, to control the crystal orientation and crystallization kinetics of the α-$FAPbI_3$-rich perovskite throughout both the nucleation and growth processes. The localized and embedded 2D perovskite at the top interior surface of the wet perovskite film serves as a templet, inducing the growth of the α-$FAPbI_3$-rich perovskites with high film quality and large grain size. The corresponding perovskite film can also passivate bulk and surface defects, suppress nonradiative recombination within the film, resulting in an ultralong carrier lifetime exceeding 27 µs. As a result, the PSCs fabricated through this method exhibit a high PCE of 26.16% (certified 25.84%) and an impressive V_{OC} of 1.213 V, along with outstanding operational stability as well as excellent high and low temperature cycle stability.

Supporting Information

Supporting Information is available from the Wiley Online Library or from the author.

Acknowledgements

The authors gratefully acknowledge the financial support from the National Natural Science Foundation of China (Grant No. 52273182), the National Key Research and Development Program of China (Grant No. 2019YFA0705900), and the Natural Science Foundation of Hebei Province (Grant No. B2022408005). They are thankful for the beam time provided by the 1W1A station (Beijing Synchrotron Radiation Facility) for GIWAXS characterization.

Conflict of Interest

The authors declare no conflict of interest.

Data Availability Statement

The data that support the findings of this study are available from the corresponding author upon reasonable request.

Keywords

2D perovskite, crystal orientation, morphology, perovskite solar cells, stability

Received: April 25, 2024
Revised: June 8, 2024
Published online:

[1] S. H. Turren-Cruz, A. Hagfeldt, M. Saliba, *Science* **2018**, *362*, 449.
[2] H. Min, M. Kim, S.-U. Lee, H. Kim, G. Kim, K. Choi, J. H. Lee, S. I. Seok, *Science* **2019**, *366*, 749.
[3] Y. Zhao, F. Ma, Z. Qu, S. Yu, T. Shen, H. X. Deng, X. Chu, X. Peng, Y. Yuan, X. Zhang, J. You, *Science* **2022**, *377*, 531.
[4] J. Park, J. Kim, H. S. Yun, M. J. Paik, E. Noh, H. J. Mun, M. G. Kim, T. J. Shin, S. I. Seok, *Nature* **2023**, *616*, 724.
[5] T. Bu, J. Li, H. Li, C. Tian, J. Su, G. Tong, L. K. Ono, C. Wang, Z. Lin, N. Chai, X. L. Zhang, J. Chang, J. Lu, J. Zhong, W. Huang, Y. Qi, Y. B. Cheng, F. Huang, *Science* **2021**, *372*, 1327.
[6] H. Lu, Y. Liu, P. Ahlawat, A. Mishra, W. R. Tress, F. T. Eickemeyer, Y. Yang, F. Fu, Z. Wang, C. E. Avalos, B. I. Carlsen, A. Agarwalla, X. Zhang, X. Li, Y. Zhan, S. M. Zakeeruddin, L. Emsley, U. Rothlisberger, L. Zheng, A. Hagfeldt, M. Gratzel, *Science* **2020**, *370*, eabb8985.
[7] B.-w. Park, H. W. Kwon, Y. Lee, D. Y. Lee, M. G. Kim, G. Kim, K.-j. Kim, Y. K. Kim, J. Im, T. J. Shin, S. I. Seok, *Nat. Energy* **2021**, *6*, 419.
[8] W. Hui, L. Chao, H. Lu, F. Xia, Q. Wei, Z. Su, T. Niu, L. Tao, B. Du, D. Li, Y. Wang, H. Dong, S. Zuo, B. Li, W. Shi, X. Ran, P. Li, H. Zhang, Z. Wu, C. Ran, L. Song, G. Xing, X. Gao, J. Zhang, Y. Xia, Y. Chen, W. Huang, *Science* **2021**, *371*, 1359.

[9] P. J. Shi, Y. Ding, B. Ding, Q. Y. Xing, T. Kodalle, C. M. Sutter-Fella, I. Yavuz, C. L. Yao, W. Fan, J. Z. Xu, Y. Tian, D. Y. Gu, K. Zhao, S. Tan, X. Zhang, L. B. Yao, P. J. Dyson, J. L. Slack, D. R. Yang, J. J. Xue, M. K. Nazeeruddin, Y. Yang, R. Wang, *Nature* **2023**, *620*, 323.
[10] S. Wang, T. Yang, Y. Yang, Y. Du, W. Huang, L. Cheng, H. Li, P. Wang, Y. Wang, Y. Zhang, C. Ma, P. Liu, G. Zhao, Z. Ding, S. F. Liu, K. Zhao, *Adv. Mater.* **2023**, *35*, 2305314.
[11] J. W. Lee, Z. Dai, T. H. Han, C. Choi, S. Y. Chang, S. J. Lee, N. De Marco, H. Zhao, P. Sun, Y. Huang, Y. Yang, *Nat. Commun.* **2018**, *9*, 3021.
[12] J. W. Lee, S. Tan, T. H. Han, R. Wang, L. Zhang, C. Park, M. Yoon, C. Choi, M. Xu, M. E. Liao, S. J. Lee, S. Nuryyeva, C. Zhu, K. Huynh, M. S. Goorsky, Y. Huang, X. Pan, Y. Yang, *Nat. Commun.* **2020**, *11*, 5514.
[13] S. Song, S. J. Yang, W. Choi, H. Lee, W. Sung, C. Park, K. Cho, *Adv. Energy Mater.* **2020**, *10*, 2001759.
[14] T. Zhou, H. Lai, T. Liu, D. Lu, X. Wan, X. Zhang, Y. Liu, Y. Chen, *Adv. Mater.* **2019**, *31*, 1901242.
[15] T. Zhou, Z. Xu, R. Wang, X. Dong, Q. Fu, Y. Liu, *Adv. Mater.* **2022**, *34*, 2200705.
[16] C. Luo, G. Zheng, F. Gao, X. Wang, Y. Zhao, X. Gao, Q. Zhao, *Joule* **2022**, *6*, 240.
[17] J. Guo, B. Wang, D. Lu, T. Wang, T. Liu, R. Wang, X. Dong, T. Zhou, N. Zheng, Q. Fu, Z. Xie, X. Wan, G. Xing, Y. Chen, Y. Liu, *Adv. Mater.* **2023**, *35*, 2212126.
[18] Y. Zhao, H. Tan, H. Yuan, Z. Yang, J. Z. Fan, J. Kim, O. Voznyy, X. Gong, L. N. Quan, C. S. Tan, J. Hofkens, D. Yu, Q. Zhao, E. H. Sargent, *Nat. Commun.* **2018**, *9*, 1607.
[19] M. Qin, P. F. Chan, X. Lu, *Adv. Mater.* **2021**, *33*, 2105290.
[20] S. Sidhik, Y. Wang, M. De Siena, R. Asadpour, A. J. Torma, T. Terlier, K. Ho, W. Li, A. B. Puthirath, X. Shuai, A. Agrawal, B. Traore, M. Jones, R. Giridharagopal, P. M. Ajayan, J. Strzalka, D. S. Ginger, C. Katan, M. A. Alam, J. Even, M. G. Kanatzidis, A. D. Mohite, *Science* **2022**, *377*, 1425.
[21] N. J. Jeon, J. H. Noh, W. S. Yang, Y. C. Kim, S. Ryu, J. Seo, S. I. Seok, *Nature* **2015**, *517*, 476.
[22] Q. Han, S. H. Bae, P. Sun, Y. T. Hsieh, Y. M. Yang, Y. S. Rim, H. Zhao, Q. Chen, W. Shi, G. Li, Y. Yang, *Adv. Mater.* **2016**, *28*, 2253.
[23] Y. Huang, X. Lei, T. He, Y. Jiang, M. Yuan, *Adv. Energy Mater.* **2021**, *12*, 2100690.
[24] M. Kim, G.-H. Kim, T. K. Lee, I. W. Choi, H. W. Choi, Y. Jo, Y. J. Yoon, J. W. Kim, J. Lee, D. Huh, H. Lee, S. K. Kwak, J. Y. Kim, D. S. Kim, *Joule* **2019**, *3*, 2179.
[25] J. Rivnay, S. C. B. Mannsfeld, C. E. Miller, A. Salleo, M. F. Toney, *Chem. Rev.* **2012**, *112*, 5488.
[26] J. Schlipf, P. Müller-Buschbaum, *Adv. Energy Mater.* **2017**, *7*, 1700131.
[27] J. M. Hoffman, I. Hadar, X. Li, W. Ke, E. S. Vasileiadou, J. Strzalka, L. X. Chen, M. G. Kanatzidis, *Chem* **2022**, *8*, 1067.
[28] D. Lu, G. Lv, Z. Xu, Y. Dong, X. Ji, Y. Liu, *J. Am. Chem. Soc.* **2020**, *142*, 11114.
[29] R. Azmi, E. Ugur, A. Seitkhan, F. Aljamaan, A. S. Subbiah, J. Liu, G. T. Harrison, M. I. Nugraha, M. K. Eswaran, M. Babics, Y. Chen, F. Xu, T. G. Allen, A. u. Rehman, C.-L. Wang, T. D. Anthopoulos, U. Schwingenschlögl, M. De Bastiani, E. Aydin, S. De Wolf, *Science* **2022**, *376*, 73.
[30] Y. Gao, X. Dong, Y. Liu, *Nano-Micro Lett.* **2023**, *15*, 169.
[31] Q. Jiang, Y. Zhao, X. Zhang, X. Yang, Y. Chen, Z. Chu, Q. Ye, X. Li, Z. Yin, J. You, *Nat. Photonics* **2019**, *13*, 460.
[32] L. Canil, T. Cramer, B. Fraboni, D. Ricciarelli, D. Meggiolaro, A. Singh, M. Liu, M. Rusu, C. M. Wolff, N. Phung, Q. Wang, D. Neher, T. Unold, P. Vivo, A. Gagliardi, F. De Angelis, A. Abate, *Environ. Sci.* **2021**, *14*, 4858.
[33] F. Ansari, E. Shirzadi, M. Salavati-Niasari, T. LaGrange, K. Nonomura, J. H. Yum, K. Sivula, S. M. Zakeeruddin, M. K. Nazeeruddin, M. Gratzel, P. J. Dyson, A. Hagfeldt, *J. Am. Chem. Soc.* **2020**, *142*, 11428.
[34] J. J. Yoo, G. Seo, M. R. Chua, T. G. Park, Y. Lu, F. Rotermund, Y. K. Kim, C. S. Moon, N. J. Jeon, J. P. Correa-Baena, V. Bulovic, S. S. Shin, M. G. Bawendi, J. Seo, *Nature* **2021**, *590*, 587.
[35] H. Cho, S. H. Jeong, M. H. Park, Y. H. Kim, C. Wolf, C. L. Lee, J. H. Heo, A. Sadhanala, N. Myoung, S. Yoo, S. H. Im, R. H. Friend, T. W. Lee, *Science* **2015**, *350*, 1222.
[36] L. Yang, H. Zhou, Y. Duan, M. Wu, K. He, Y. Li, D. Xu, H. Zou, S. Yang, Z. Fang, S. Liu, Z. Liu, *Adv. Mater.* **2023**, *35*, 2211545.
[37] R. Chen, J. Wang, Z. Liu, F. Ren, S. Liu, J. Zhou, H. Wang, X. Meng, Z. Zhang, X. Guan, W. Liang, P. A. Troshin, Y. Qi, L. Han, W. Chen, *Nat. Energy* **2023**, *8*, 839.